Faraday Discussions

Cite this: DOI: 10.1039/d1fd00015b

ROYAL SOCIETY OF CHEMISTRY

PAPER

View Article Online
View Journal

Spiers Memorial Lecture: Introduction to ultrafast spectroscopy and imaging of photochemical reactions

Toshinori Suzuki

Received 9th February 2021, Accepted 16th March 2021
DOI: 10.1039/d1fd00015b

A brief overview is presented on ultrafast spectroscopy and imaging of photochemical reactions by highlighting several experimental studies reported in the last five years. A particular focus is placed on new experiments performed using high-order harmonic generation, X-ray free electron lasers, and relativistic electron beams. Exploration of fundamental chemical reaction dynamics using these advanced experimental methodologies is in an early stage, and exciting new research opportunities await in this rapidly expanding and advancing research field. At the same time, there is no experimental methodology that provides all aspects of the electronic and structural dynamics in a single experiment, and investigations using different methodologies with various perspectives need to be considered in a comprehensive manner.

I. Introduction

Chemists have unravelled the atomistic details of invisible chemical reaction mechanisms using imagination and logical thinking based on carefully designed control experiments. It is a longstanding dream of chemists and students to be able to watch chemical reactions directly and understand their mechanisms. The most useful instrument for watching invisibly small objects is a microscope, and the technology of microscopy has advanced dramatically. Electron microscopy, which utilizes the ultrashort wavelength of matter waves, has provided us with extremely high spatial resolution that is unachievable using conventional optical microscopy. In 2020, two research groups reported that the resolution of single-particle cryo-electron microscopy[1–3] has reached a remarkable spatial resolution of 1.2 Å.[4,5] Cryo-electron microscopy is a revolutionary tool for structural biology, as it enables structural determination of biomolecules and their assemblies without crystallization. Previously, X-ray crystallography has been most widely employed for structural determination of biological samples; however, an obstacle was that high-quality crystalline samples, which are required for this

Department of Chemistry, Graduate School of Science, Kyoto University, Kyoto 606-8502, Japan. E-mail: suzuki@kuchem.kyoto-u.ac.jp

method, are very difficult to prepare for important samples such as membrane proteins. The 2017 Nobel Prize in Chemistry was awarded to three researchers who pioneered cryo-electron microscopy. Scanning tunnelling microscopy[6] and atomic force microscopy[7] were developed in the 1980s, and they have enabled us to "touch" a molecule adsorbed on a solid surface with a thin metallic needle and to determine its molecular structure. Furthermore, recently developed tip-enhanced Raman spectromicroscopy further utilizes the metallic needle as both an antenna and a focusing lens for radiation to perform spatial mapping of the spontaneous Raman intensity with atomic resolution. When the metal tip is carefully placed just above a molecule within a vertical distance of 2 Å, the radiation field is strongly localized in an extremely narrow spatial region and the Raman spectrum of the molecule becomes dependent on the tip position. Fig. 1 shows the two-dimensional maps of individual Raman band intensity measured by scanning the tip over a Co(II)–tetraphenyl porphyrin molecule adsorbed on an ultracold copper surface. These two-dimensional patterns of the spontaneous Raman intensity are reminiscent of the normal modes of molecular vibration corresponding to these Raman frequencies; more precisely, the patterns reflect the modulation amplitude of a local electronic wavefunction caused by vibrational motion.[8,9] The advances and performance of these microscopy techniques are truly impressive. On the other hand, current microscopy techniques do not have sufficient temporal resolution to track ultrafast structural changes during chemical reactions that occur on a femtosecond time scale. The desire for real-time observations of chemical reactions has led to continuous efforts to develop more advanced ultrafast spectroscopy and imaging methods for studying photoinduced molecular processes.

Over the last half-century, the shortest temporal duration of a laser pulse has been reduced by more than nine orders of magnitude, from nanoseconds to

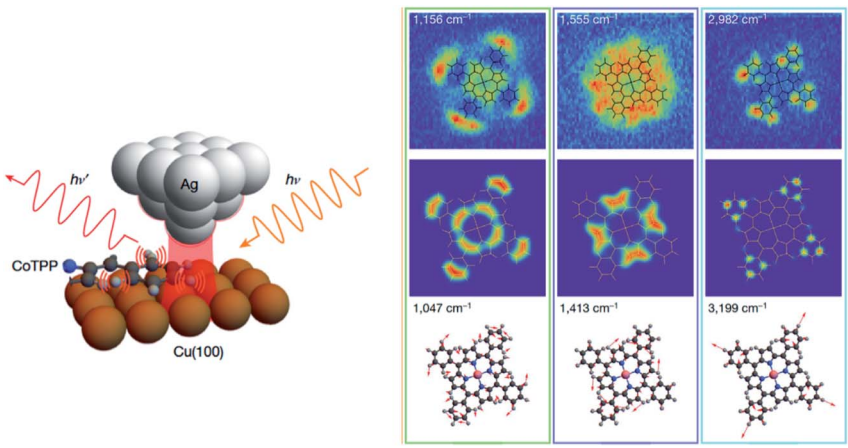

Fig. 1 Tip-enhanced Raman Spectromicroscopy (TERS): (left) schematic of TERS of a Co(II)–tetraphenyl porphyrin molecule on Cu(100) at 6 K. The silver tip acts as a focusing lens with a Gaussian waist and as a radiating antenna. (Right) top: experimental images recorded by monitoring the Raman scattering for the indicated vibrational frequencies. The images are overlaid with the molecular frameworks. Middle: theoretical simulations. Bottom: computed normal-mode vibrations. Adapted from ref. 8.

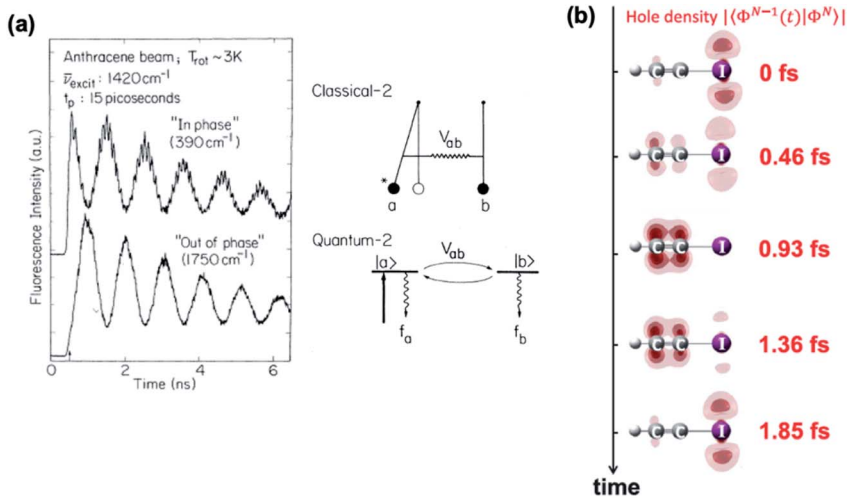

Fig. 2 Quantum beats: (a) fluorescence intensity decay profiles after coherent excitation of multiple vibronic bands of jet-cooled anthracene. Different emission bands were monitored for the two cases. The illustration shows coupling of two classical oscillators or two quantum states. (b) Charge migration in a superposition state of the D_0 and D_1 cationic states of iodoacetylene. The illustration shows periodic movement of an electron hole between the I atom and the acetylenic part. Adapted from ref. 15 and 16.

attoseconds.[10–12] (Electron pulse durations have also been reduced to attoseconds.[13,14]) In 1984, Felker and Zewail observed vibrational quantum beats created by coherent excitation of multiple vibronic states of S_1 anthracene with 15 ps pulses (Fig. 2(a)).[15] The characteristic oscillatory features of the fluorescence signals indicate that two oscillators interact with each other and exchange their vibrational energies. In 2015, Kraus *et al.* demonstrated coherent superposition of the ground (D_0) and the first excited (D_1) states of iodoacetylene cations separated by 2.23 eV using strong field ionization, and observed electronic quantum beats with a period of 1.85 fs, during which nuclear motion is essentially frozen.[16] This electronic quantum beat corresponds to periodic motion of an electron hole in the cation; the electron hole is initially localized at the iodine atom at 0 fs, and it migrates into the acetylenic part and then returns to the iodine atom after 1.85 fs. At the forefront of metrology, attosecond spectroscopy is paving a new avenue for studying electron dynamics in matter, such as charge migration, photoionization delay, and electron current in a molecule.[11,17–19] On the other hand, the time scale for atomic motion in chemical reactions is from femtoseconds to picoseconds, as determined by the atomic masses and the forces acting on the atoms; the shortest vibrational periods for chemical bonds such as C–H and O–H are approximately 10 fs. Therefore, important targets of research such as internal conversion, photoisomerization, ring-opening, charge transfer, and solvation are in the femtosecond time range.[20,21] From a technical viewpoint, it is not at all trivial to generate deep ultraviolet (UV) pulses with temporal durations much less than 10 fs,[22] so ultrafast spectroscopy in the deep UV region requires further innovation. There are many more challenging problems and room for further development.

High-order harmonic generation (HHG) and X-ray free electron lasers (XFELs) provided significant influences in ultrafast spectroscopy in the extreme UV and X-

ray regions. Exploration of chemical reaction dynamics with these methods is still in an early stage, and exciting new research opportunities await in this rapidly expanding and advancing research field. HHG utilizes an oscillating electric field of a strong laser pulse to induce tunnel ionization of rare gas atoms, acceleration of emitted photoelectrons, and coherent recombination of the photoelectrons and photoions, and it generates a burst of radiation from the extreme UV to the soft X-ray region.[23,24] On the other hand, XFELs are large-scale linear accelerators, with a length of several hundred meters to kilometers, to generate a relativistic beam of electrons and inject it into an undulator, in which an intense X-ray pulse is generated by self-amplification of stimulated emission of radiation (SASE).[25] The development of XFELs and HHG led to many breakthroughs in experimental research on photoinduced chemical dynamics. For example, prior to the realization of XFELs, ultrafast X-ray experiments were primarily limited by the pulse duration of synchrotron radiation, which is of the order of 50–100 ps, except for a few experiments performed using a slicing technique.[26–28] However, femtosecond spectroscopy in the hard X-ray region can now be routinely performed with XFELs.

A photoabsorption spectrum provides some valuable information on the photoinduced dynamical processes, because the spectrum corresponds to the Fourier transform of the autocorrelation function $\langle\Psi(0)|\Psi(t)\rangle$ of the nuclear wave packet $\Psi(t)$ in the excited electronic state.[29] Photoexcitation with an ultrashort optical pulse creates a replica of the ground-state vibrational wave function on the excited-state potential energy surface, and this spatially localized vibrational (nuclear) wave function (or wave packet) evolves with time according to the potential gradient. If the nuclear wave packet prepared on the excited state potential energy surface leaves the Franck–Condon region and never returns, $\langle\Psi(0)|\Psi(t)\rangle$ diminishes rapidly with time and the corresponding absorption spectrum exhibits a broad band feature. On the other hand, the spectrum reveals clear vibrational structures if the wave packet repeatedly returns at least in part to the Franck–Condon region. Thus, absorption spectroscopy enables us to decode information concerning the nuclear wave packet dynamics at the outset of photo-induced dynamics, if the intrinsic spectral features are not obscured by spectral broadening due to hot bands (transitions from an ensemble of thermally populated levels) and/or inhomogeneous broadening (due to differences in the local solvation environment in a solution). On the other hand, ultrafast pump–probe spectroscopy enables tracking of entire photochemical reactions from the Franck–Condon region to the final product and provides far more information on the electronic and structural dynamics in photochemical reactions. These two viewpoints are complementary and indispensable for understanding the chemical reaction.

Observation of electronic dynamics is certainly important for understanding electron transfer and redox reactions.[30] Moreover, elucidation of electronic dynamics is generally important for understanding photochemical reactions, because these reactions often proceed *via* non-adiabatic transitions between different electronic states.[31–34] The non-adiabatic transition is observed as the breakdown of the Born–Oppenheimer (or adiabatic) approximation that separates nuclear and electron motion in the quantum mechanical description of a molecule. When this approximation holds, a chemical reaction is regarded as quantum wave packet motion of nuclei on a single potential energy surface, for example, the ground-state surface. However, a photochemical reaction begins at

one of the excited-state potential energy surfaces reached by photoabsorption, and surface crossings between the excited and ground states are ubiquitous. In the vicinities of these crossings, the Born–Oppenheimer approximation inevitably breaks down and non-adiabatic transitions between the potential energy surfaces occur. These transitions "create" new reaction paths, which are not anticipated in the framework of the Born–Oppenheimer approximation. As an example, a photochemical ring-opening reaction of 1,3-cyclohexadiene (CHD) to form 1,3,5-hexatriene (HT) is schematically shown in Fig. 3. This reaction is involved in producing previtamin D in our skin under sunlight and is also one of the best-known examples of the Woodward–Hoffmann rule regarding the chemical reaction pathway dictated by molecular orbital symmetry.[35–37] As shown in Fig. 3, the potential energy surface for the first excited state of CHD accessed by UV absorption is not adiabatically correlated to the ground state of HT, so non-adiabatic transitions must be involved in this reaction. The characteristic feature of this reaction is that the HOMO and LUMO of CHD are correlated with the LUMO and HOMO of HT, respectively; therefore, the energy ordering of the HOMO and LUMO is reversed during this reaction. The ground state of HT has double occupancy of the 11b orbital, and it is correlated with the doubly excited S_2^{**} state of CHD. Therefore, the ring-opening reaction from the S_1 state of CHD is induced by non-adiabatic transitions through the S_1–S_2 and S_1–S_0 conical intersections of the potential energy surfaces.[38] The concept of non-adiabatic transitions is well known for one-dimensional systems, and a simple analytical (Landau–Zener) formula approximating the non-adiabatic transition probability is described in textbooks on quantum mechanics. On the other hand, the non-adiabatic dynamics in the high-dimensional configuration space of polyatomic molecules are highly complex, and their understanding requires accurate computation of the potential energy hypersurfaces and experimental measurements of various observables regarding electronic dynamics.

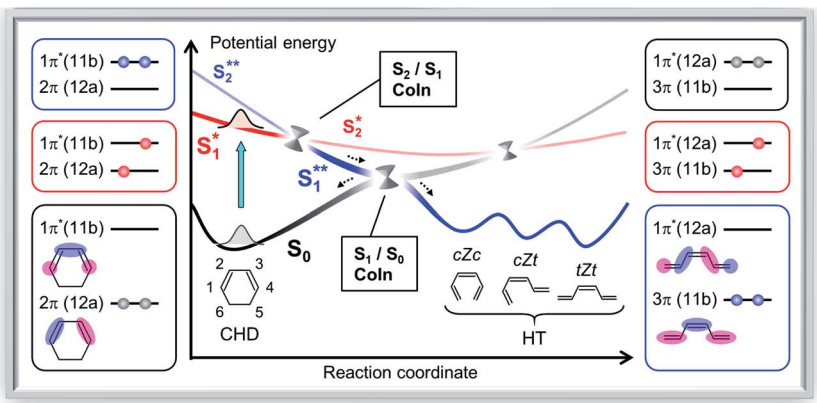

Fig. 3 Non-adiabatic dynamics in the photochemistry of CHD: qualitative presentation of the potential energy curves involved in the ring-opening reaction of CHD. C_2 symmetry notation is presented to clarify the correlation among the molecular orbitals. However, the reaction path preserving C_2 symmetry leads to a strongly avoided crossing with a large S_1/S_0 energy gap. Therefore, the reaction proceeds through the S_1/S_0 conical intersection with non-C_2 symmetry. HT has three isomers as indicated.

Elucidation of the structural dynamics of photoexcited molecules is essential for understanding their properties and functions. Structural biology elucidates the physiological functions of biomolecules from their shapes. In organic chemistry, the beautiful geometrical structures of crown ethers[39] and BINAP–metal complex catalysts[40] provide highly useful functions. The *cis–trans* photoisomerization of retinal provides us with our ability to see. Although transient absorption spectroscopy and photoelectron spectroscopy are most useful for elucidating electronic dynamics, it is generally difficult to determine complex molecular structures with these spectroscopic methods. Ultrafast X-ray/electron diffraction methods (diffraction from a disordered sample is termed scattering but has the same meaning) that directly determine interatomic distances in molecules play an invaluable role in elucidating structural dynamics in chemical reactions.[41–48] Historically, electron diffraction has made a significant contribution as a methodology for accurate determination of molecular structures in the ground electronic state. For example, Fig. 4(a) shows the electron diffraction pattern recorded for gaseous CCl_4 in the 1950s,[49] revealing beautiful interferences among the electron waves scattered by carbon and chlorine atoms. The interatomic distances were extracted from this pattern as shown in Fig. 4(b), which clearly shows two peaks corresponding to the C–Cl and Cl–Cl interatomic distances. The great advantage of diffraction experiments is that interatomic distances (or their distribution functions) can be determined. Ultrafast X-ray/electron diffraction probes the transient structure of a molecule with the same principle. Elastic X-ray scattering is caused by oscillation of electrons in an X-ray radiation field (Thomson scattering), while elastic electron scattering is caused by deflection of incoming electrons by electrostatic interactions with all the electrons and nuclei in a target molecule (Rutherford scattering). Since the scattering intensity in the former case is about five orders of magnitude smaller than that in the latter case, ultrafast X-ray diffraction studies of gaseous molecules have been highly challenging. This situation has been completely changed by XFELs, which provide an X-ray photon flux (10^{12} photons per pulse) that is seven orders of magnitude greater than the flux (3.7×10^4 electrons per pulse) of an electron beam.[50] The signal intensity in ultrafast X-ray diffraction measurements has

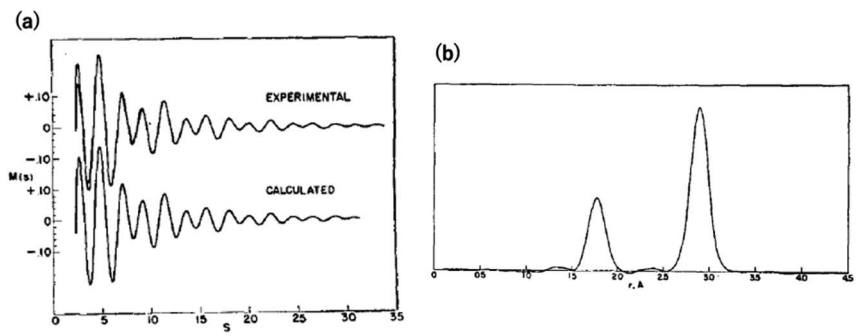

Fig. 4 Conventional electron diffraction experiment: (a) experimental and calculated electron diffraction patterns for CCl_4. (b) Radial distribution function (interatomic distances) extracted from the data shown in (a). The shorter distance corresponds to C–Cl and the longer one corresponds to Cl–Cl. Adapted from ref. 49.

become even greater than that in ultrafast electron diffraction (UED) measurements.[48] In electron and X-ray diffraction experiments, the results are usually analysed using an independent atom model (IAM), which views a molecule as an array of spherical atoms and predicts the overall diffraction signal expected for the molecule from the scattering power (atomic form factors) of individual atoms. The IAM does not consider the formation of chemical bonds, polarization or electronic excitation. Some recent studies employ quantum chemical calculations of molecular electronic states for the analysis, and this will be a standard way of analysis in the future.

A nuclear wave packet on the excited-state potential energy surface gradually disperses as it propagates. Moreover, it even spreads over multiple potential energy surfaces *via* spin–orbit and non-adiabatic (vibronic) coupling. Internal conversion to the ground state also leads to branching into different chemical structures. Thus, the probability density distribution for nuclei becomes more and more diverse as the reaction proceeds, although it remains a quantum mechanical superposition (Schrödinger's cat) prior to decoherence. A broad nuclear probability density distribution generally prevents a clear diffraction pattern from being obtained, making structural determination more challenging. In these cases, wave packet or classical trajectory calculations on *ab initio* potential energy surfaces can be employed for the analysis of experimental results.

II. Photochemical reactions of isolated molecules

In retrospect, it was the *Faraday Discussion* in 1999 where the author presented the first experimental report on time-resolved photoelectron imaging (TRPEI).[51,52] Therefore, I will begin with this memorable topic. We attempted real-time observation of ultrafast S_2 $^1B_{2u}(\pi, \pi^*) \rightarrow S_1$ $^1B_{3u}(n, \pi^*)$ internal conversion in pyrazine. Pyrazine is one of the best-known examples of molecules that undergo ultrafast internal conversion through the conical intersections of the potential energy surfaces, and has been studied as a benchmark system by many theorists.[31,34] For example, Seel and Domcke presented model calculations for time-resolved photoelectron spectroscopy[53,54] of $S_2 \rightarrow S_1$ internal conversion in pyrazine.[55] However, the temporal resolution of our experiment in 1999 was only 0.2–0.3 ps, which was insufficient for real-time observation of $S_2 \rightarrow S_1$ internal conversion which was theoretically predicted to occur in less than 30 fs. As an alternative, we observed the $S_1 \rightarrow T_1$ $^3B_{3u}(n, \pi^*)$ intersystem crossing, which was a well-known intermediate coupling case of radiationless molecular transition.[52] Subsequently, filamentation four-wave mixing (FFWM) in a noble gas enabled us to generate ultrashort pulses at 264 and 198 nm and improved the instrumental time resolution to 22 fs.[56] TRPEI using FFWM successfully identified $S_2 \rightarrow S_1$ internal conversion that occurs with a time constant of 22 fs based on the ultrafast change in photoelectron angular anisotropy.[57] We have further shortened the FFWM wavelength to 133 nm (9.3 eV) in order to observe the entire cascaded electronic dephasing process from the S_2 state of pyrazine, including $S_1 \rightarrow T_1$ intersystem crossing and $S_1 \rightarrow S_0$ internal conversion.[58,59]

Fig. 5 shows two-dimensional (2D) slices through the 3D velocity distributions of photoelectrons obtained using 264 nm pump and 133 nm probe pulses. The

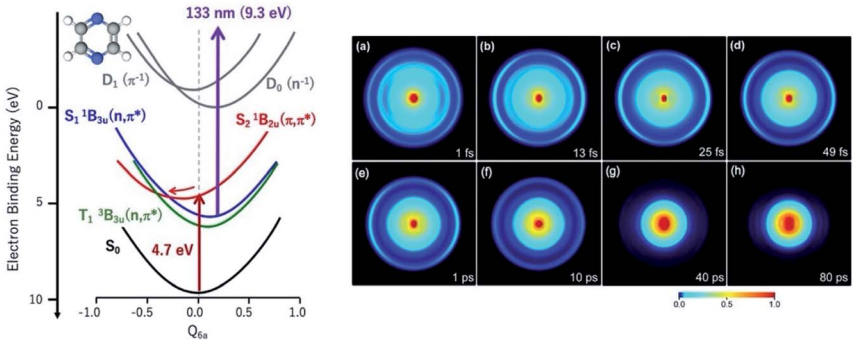

Fig. 5 Time-resolved photoelectron imaging spectroscopy: (left) 1D slice of the potential energy surfaces of the pyrazine molecule. The potential energy curves along the totally symmetric 6a mode indicate a conical intersection between $S_2(\pi,\pi^*)$ and $S_1(n,\pi^*)$. (Right) 2D slices through the 3D photoelectron scattering distributions. The initial excitation occurs to the S_2 state, ultrafast internal conversion to S_1 occurs within 22 fs, and further relaxation to T_1 and S_0 occurs. 133 nm photons can induce ionization from all electronic states. 2D slices through the 3D photoelectron scattering distributions were obtained at (a) 1, (b) 13, (c) 25 and (d) 49 fs, and (e) 1, (f) 10, (g) 40 and (h) 80 ps. The photoemission signals in (a) and (b) are primarily from S_2, those in (d) and (e) are from S_1, and the photoemission signal in (h) is from T_1 and S_0. The directions of the polarization vectors for the 264 and 133 nm pulses are parallel to each other and both are in the vertical direction in the plane of the figure. Adapted from ref. 59.

pump wavelength is resonant with the $S_2 \leftarrow S_0$ absorption band near the origin. The probe photon energy is almost the same as the ionization energy of pyrazine; therefore, all electronic states involved in cascaded electronic dephasing from the S_2 state can be detected using the 133 nm probe pulses. Close examination of the images between 0 and 49 fs reveals the disappearance of the intermediate velocity component, indicating the occurrence of internal conversion from S_2 to S_1. The photoelectron signal also reveals a vibrational quantum beat in the totally symmetric (accepting) mode ν_{6a} in S_1 (not shown here). Further relaxation from S_1 to T_1 and S_0 is seen from the clear variation of the images between 1 and 40 ps. The formation of S_0 is the end of the photophysical process but not of the photochemical reaction of pyrazine. The highly vibrationally excited pyrazine in S_0 ultimately undergoes three-body dissociation into HCN and acetylene.[60] The dissociation, however, occurs on a sub-millisecond time scale, which is far beyond the observation time window of TRPEI. Some researchers suggest that the $^1A_u(n, \pi^*)$ state is also involved in the dynamics; however, its importance has been evaluated differently depending on the computational methods.[61–64]

Fig. 6(a) is a photoelectron spectrum for the S_2 state extracted from the photoelectron images. There are three strong bands. The red (D_1) and green (D_x) bands correspond to photoemission of the electrons indicated by the same colour in the $\pi\pi^*$ electron configuration shown in Fig. 6(b); these are allowed transitions for the $\pi\pi^*$ configuration $[(1b_{2g})^2(5b_{1u})^2(1b_{1g})^1(6a_g{}^2)(2b_{3u})^1]$. On the other hand, the blue (D_3) band in Fig. 6(a) is an ionization transition not expected for this configuration and is ascribed to ionization from a different electron configuration of $[(1b_{2g})^1(5b_{1u})^2(1b_{1g})^2(6a_g)^2(1a_u)^1]$ (Fig. 6(b)). Therefore, the blue band indicates the presence of a configuration interaction in the S_2 state. The CI coefficients for

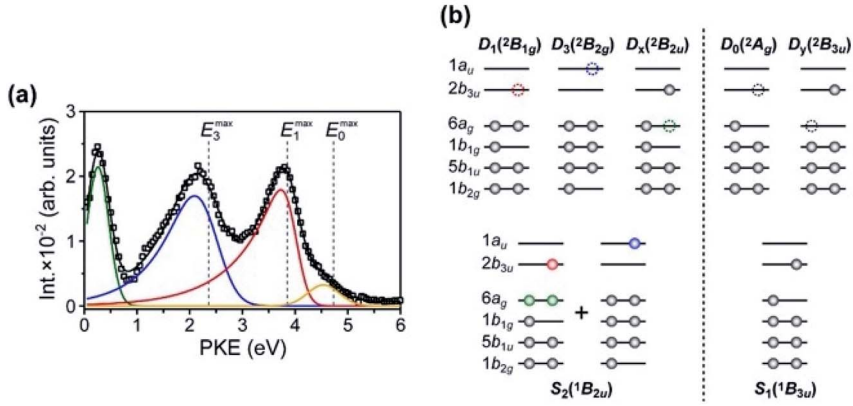

Fig. 6 Influence of configuration interaction: (a) photoelectron kinetic energy (PKE) distribution measured for the short-lived S_2 state prepared by 264 nm photoexcitation from S_0 and 133 nm ionization with a short delay time. The observed photoelectron spectrum is fitted using four bands indicated in different colours. (b) Electron configurations in S_1, S_2, D_0, D_1, D_3, D_x, and D_y. S_2 has two major electron configurations due to b_{1g}–b_{3u} and b_{2g}–a_u electron promotion, which is contrasted with S_1 characterized by a single electron configuration. The photoelectron bands coloured in red, blue and green in (a) arise from the removal of an electron indicated in the same colour from one of the two electron configurations in S_2. The PKEs for D_1–S_2 and D_x–S_2 are almost the same as those for D_0–S_1 and D_y–S_1. Therefore, the photoelectron images in Fig. 5(a) and (d) look similar except for the distribution corresponding to the D_3–S_2 band. Adapted from ref. 59.

the former and latter configurations were determined to be 0.70 and 0.54, respectively, in a computational study by Hackmeyer and Whitten in 1971,[65] and 0.69 and 0.45, respectively, by Mignolet *et al.*[64] The photoelectron images (a) and (e) in Fig. 5 are of ionization from $S_2(\pi, \pi^*)$ and $S_1(n, \pi^*)$, respectively. When we compare these two images, the only noticeable difference is the presence and absence of the intermediate component discussed above; the velocity components seen in Fig. 5(e) are also present in (a). This is because these two photoelectron signals correspond to photoemission from the $2b_{3u}$ and $6a_g$ molecular orbitals. These orbitals are occupied in both $S_2(\pi, \pi^*)$ and $S_1(n, \pi^*)$ (Fig. 6(b)), so photoemission from these two orbitals provides very similar photoelectron kinetic energy distributions for $S_2(\pi, \pi^*)$ and $S_1(n, \pi^*)$. Thus, disappearance of the blue-colored D_3 band in Fig. 6(a) served as an unambiguous marker for the ultrafast $S_2 \rightarrow S_1$ internal conversion in TRPEI with 133 nm probe pulses.

Pyrazine remains a benchmark system for studies of non-adiabatic transitions; the sensitivities of other spectroscopic methods, such as fluorescence up-conversion, transient absorption, two-dimensional electronic, and X-ray absorption spectroscopy (NEXAFS: near edge X-ray absorption fine structure), to non-adiabatic dynamics have been theoretically discussed using pyrazine as an example.[66–69]

In addition to FFWM, HHG is highly useful for ultrafast photoelectron spectroscopy with extreme UV radiation.[70] A seeded free electron laser is also employed for ultrafast pump–probe photoelectron spectroscopy in combination with a synchronized table-top femtosecond laser.[71] Since photoelectron spectroscopy is highly vulnerable to space charge effects,[72–74] active research and

development related to HHG light sources driven by high-repetition-rate lasers are underway in many laboratories, aiming at space-charge-free measurements.[75–77]

In the remaining part of this section, I would like to introduce recent progress in experimental studies on photochemical reactions in the gas phase, by taking examples mainly for the ring-opening reaction of CHD shown in Fig. 3. The first example is time-resolved NEXAFS (near edge X-ray absorption fine structure) spectroscopy. This is analogous to UV/VIS transient absorption spectroscopy, which probes valence–valence transitions, but NEXAFS corresponds to electronic transitions from inner-shell to valence orbitals. Since the energies of inner-shell orbitals significantly change with atomic number (or nuclear charge), so do their transition energies, making NEXAFS element-selective.[30] Several groups demonstrated time-resolved NEXAFS spectroscopy with table-top HHG light sources in the carbon K-edge (284 eV) region.[78,79] Attar *et al.* excited CHD with UV light to induce the ring-opening reaction of CHD, and they observed electronic transitions from C(1s) to the HOMO and higher orbitals.[79] The transition to the HOMO is also allowed, because UV excitation induces the HOMO(12a)–LUMO(11b) transition, creating a single hole in the HOMO. The black line in Fig. 7(A) shows the NEXAFS spectrum calculated for the ground state of CHD, while the red line is for the Franck–Condon region in the photoexcited state (S_1^*). Since photoexcited CHD undergoes ultrafast molecular deformation along the ring-opening reaction coordinate, the energies of the LUMO and HOMO change rapidly. Consequently, the HOMO and LUMO are considered degenerate in the middle of the ring-opening reaction. The experimental results shown in Fig. 7(B) do not clearly reveal an ultrafast energy shift of the HOMO band; however, the observed spectra exhibit a feature at around 282 eV that is consistent with the expected coalescence of the HOMO and LUMO bands. Currently, many research groups are trying to implement similar soft X-ray spectrometers based on HHG,

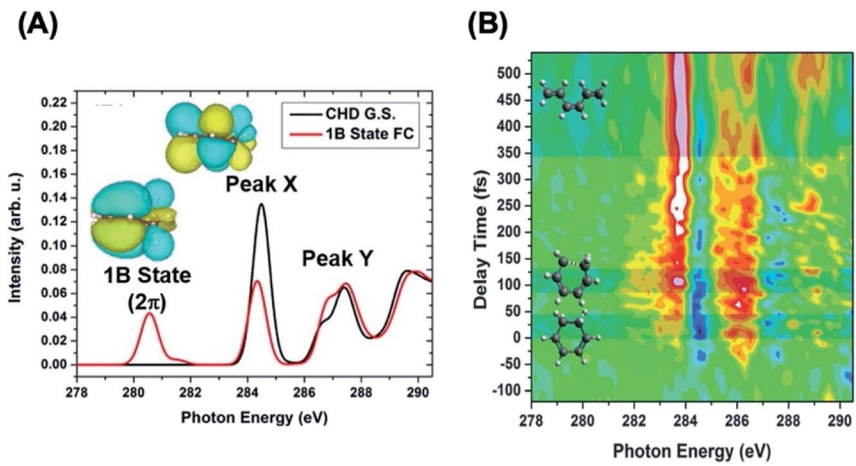

Fig. 7 X-ray absorption spectroscopy (NEXAFS): (A) soft X-ray absorption spectra of CHD calculated for the ground state (black) and the first excited state (red). (B) Transient absorption spectra of CHD measured experimentally with a pump wavelength of 266 nm. Adapted from ref. 79.

and the performance of these instruments is expected to be further improved in terms of the temporal resolution and S/N ratio. The element selectivity provided by NEXAFS will also be useful for studying solution chemistry. For example, in the case of an aqueous solution, inner-shell absorption by oxygen atoms occurs around 530 eV; therefore, element-selective spectroscopy can be performed, for example for carbon- and nitrogen-containing solutes, in aqueous solutions using the absorption window of liquid water ("water window").

While time-resolved NEXAFS spectroscopy probes the time-evolution of unoccupied valence orbitals using electronic transitions from inner-shell orbitals, time-resolved photoelectron spectroscopy (TRPES) probes occupied orbitals using the photoelectric effect. In a forthcoming paper by Karashima *et al.*, they have employed TRPES using the XUV probe pulses (21.7 eV) generated by HHG to explore the ring-opening reaction of CHD.[80] Since the photon energy of XUV radiation exceeds the ionization energies of all chemical species involved in the reaction, it enables observation of the entire electronic dynamics from the Franck–Condon region of CHD to the final products of HT and CHD. They combined the XUV laser with an ultrafast DUV laser based on FFWM to achieve the pump-probe cross-correlation time. The spectra clearly revealed evolution of a non-stationary electronic state from the singly excited S_1^* state to the doubly excited S_1^{**} state within 30 fs, firmly establishing the non-adiabatic reaction mechanism mediated by the doubly excited state. The assignments of the photoelectron spectra were fully confirmed by the computed electron binding energies along the ring-opening reaction path using highly accurate quantum chemical calculations at the level of XMS-CASPT2 (extended multistate complete active space second-order perturbation theory). They also performed more thorough simulations based on full-dimensional surface hopping trajectory calculations previously reported by Polyak *et al.*[81] and the photoionization dynamics

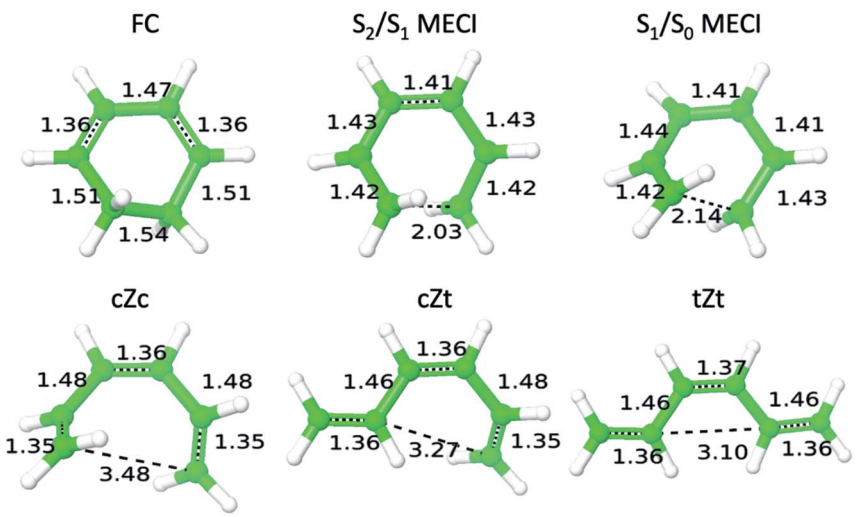

Fig. 8 Molecular deformation along the ring-opening reaction path: molecular structures calculated along the ring-opening reaction path of CHD using XMS-CASPT2. The interatomic distances are indicated in Ångström. MECI stands for the minimum energy conical intersection. Adapted from ref. 80.

calculated along these trajectories. Excellent agreement with the experimental result was found. Fig. 8 shows the molecular structures at critical nuclear configurations along the ring-opening reaction path calculated using XMS-CASPT2. One can see that CHD at the Franck–Condon point in S_1^* has two C=C double bonds as in the ground state. However, in the region between the S_2/S_1 and S_1/S_0 conical intersections, all of the carbon–carbon interatomic distances become essentially the same, except for C_5–C_6 that is going to dissociate. Considerably greater structural deformation occurs in the ground state of HT, which can be probed using electron/X-ray diffraction methods as described below.

Now we consider the methods to probe structural dynamics. The first is UED. Unlike the conventional electron diffraction experiment shown in Fig. 4 using a continuous electron beam, UED employs a pulsed electron beam, so that it is technically demanding to obtain a high signal-to-noise ratio and high temporal and spatial resolution while avoiding space-charge effects. While photoelectron spectroscopy and transient absorption spectroscopy are sensitive to electronic structures and non-adiabatic transitions, ultrafast electron/X-ray diffraction provides invaluable information on structural dynamics.[41–47,82–84] Fig. 9 presents electron diffraction data obtained using a relativistic electron beam with an energy of 3.7 MeV (corresponding to a wavelength of 0.3 pm). The atomic pair (interatomic distance) distribution function for CHD before photoexcitation shown in Fig. 9(a) is dominated by two peaks corresponding to the distances of

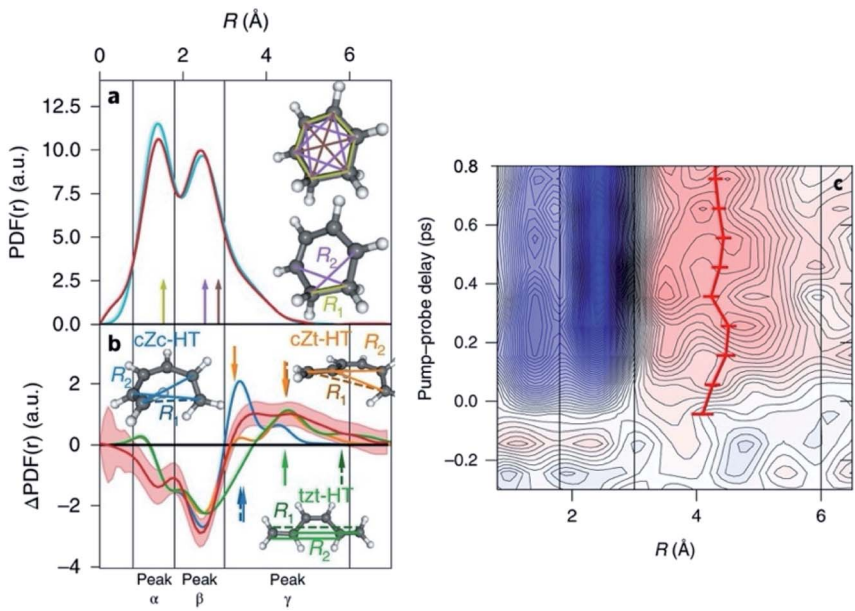

Fig. 9 Ultrafast electron diffraction: (a) experimental (red) and simulated (light blue) pair distribution functions for CHD. The two main peaks are related to R_1 and R_2 in the inset. (b) Simulated pair distribution functions for cZc-HT (blue), cZt-HT (orange), and tZt-HT (green). An experimental function for a delay time of 0.55 ps is also shown (red). (c) Experimental map of the time-evolving pair distribution function. The solid line indicates the centre of mass position in peak area γ between 3 and 6 Å. Blue and red correspond to negative and positive signals, respectively. Adapted from ref. 84.

the first and second nearest neighbour carbon atom pairs. The prominent change observed after photoexcitation is the appearance of a signal due to larger carbon–carbon distances (Fig. 9(b)), which can only be possible for HT; therefore, the enhancement of the γ peak, which refers to the signal for the interatomic distance between 3 and 6 Å, is simply due to the formation of the HT structure.[84] Comparing the time evolution of the observed γ peak with theoretical simulations revealed that the centre of mass position of the γ peak exhibits an oscillatory feature, as shown by the red line in Fig. 9(c). This oscillation is ascribed to torsional motion around the C–C single bonds newly formed by the ring-opening reaction, and it corresponds to rotational isomerization among the cZc, cZt, and tZt forms. The instrumental response function of this experiment was 160 fs. Although it is desirable to further improve the temporal resolution, UED with the current resolution is already highly useful for studying structural dynamics in various reactions.

Diffraction experiments generally do not differentiate electronic states of the target molecule, and IAM analysis of diffraction signals does not either. Yang *et al.* attempted to eliminate this limitation and investigate both the electronic and

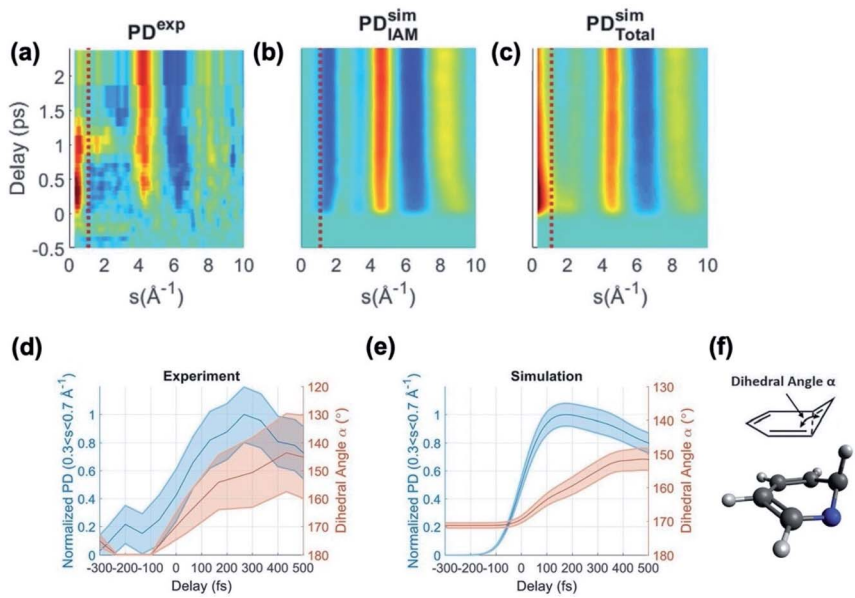

Fig. 10 Inelastic scattering during ultrafast electron diffraction: (a–c) Experimental and simulated electron diffraction signals for pyridine. (a) Experimental percentage difference (PD) signal, normalized to the 9% excitation ratio. (b) Simulated PD signal using the independent atom model (elastic component only). (c) Simulated PD total (elastic and inelastic) signal using *ab initio* electron diffraction simulation. In (a) to (c), the red dotted line denotes a momentum transfer $s = 1.1$ Å^{-1}. (d and e) Experimental (d) and simulated (e) temporal evolution of the small-angle PD signal (blue, normalized to the maximum value) and dihedral angle (red) defined in (f). The uncertainty is represented by the shaded regions, calculated as one standard deviation of a bootstrapped dataset (experiment) or one standard error of the mean (SEM) of all trajectories (simulation). (f) Definition of the dihedral angle and illustration of a plausible molecular structure. Simulation results are convolved with a 150 fs Gaussian kernel to account for the experimental instrumental response function. Adapted from ref. 44.

structural dynamics with a single UED experiment.[44,85] They excited pyridine molecules to the $S_1(n, \pi^*)$ state with 265 nm light, and investigated subsequent conformational changes and internal conversion to S_0 using UED with an instrumental time resolution of 150 fs.[44] One of the new features of their experiment was detection of inelastically scattered electrons at small scattering angles. Their results are shown in Fig. 10(a)–(c). The inelastic scattering signal is seen in Fig. 10(a) in the region of a small transfer momentum *s*. The lifetime of this signal is very short (1.1 ps) and comparable with the calculated $S_1(n,\pi^*)$ lifetime (1.3 ps), suggesting that it represents the S_1 population. Simulation based on the IAM (Fig. 10(b)) does not reproduce the inelastic scattering signal, while simulation based on the quantum chemically calculated electronic structure of pyridine (Fig. 10(c)) explains both the inelastic and elastic scattering signals.

An important dynamical feature revealed by UED is an ultrafast structural change within 500 fs. Since photoexcited pyridine has a vibrational energy of 3000 cm^{-1} in the S_1 state, the molecule overcomes a small potential barrier (640 cm^{-1}) in the ring-puckering coordinate and lifts a carbon or nitrogen atom (these elements cannot be differentiated experimentally) out of the molecular plane. This out-of-plane deformation triggers internal conversion to S_0 at a dihedral angle of 150–160°; Fig. 10(d) and (e) respectively show the experimental and computational results for the S_1 population and the dihedral angle that is defined in Fig. 10(f). The two results are in good agreement. It is noted that many theoretical studies indicated that out-of-plane deformation promotes ultrafast internal conversion in aromatic molecules such as DNA bases; however, such deformation cannot be easily identified with spectroscopic methods. Therefore, the real-time observation of out-of-plane deformation demonstrated for pyridine is of interest.[86] Ultrafast internal conversion followed by intermolecular vibrational energy transfer in solution or in biological environments prevents photochemical decomposition of a molecule; a low quantum yield for photochemical decomposition is often expressed as the photostability of a molecule.[87,88] Some researchers have suggested that photostability was the crucial property of DNA bases for recording genetic information under strong UV radiation on prebiotic Earth.[86,88,89]

Finally, Yang *et al.* ruled out the previous claim[90] that pyridine undergoes a ring-opening reaction within the observation time window.[75] It is noted that the isomerization and dissociation barriers for pyridine in the ground state have been calculated to be 90–100 kcal mol^{-1}; therefore, pyridine should undergo isomerization and dissociation if the internal energy is sufficiently large.[91] However, these processes take a long time.

Returning to the ring-opening reaction of CHD, this reaction has also been studied using X-ray diffraction, and the results elucidated another interesting aspect of the reaction. The issue here is the occurrence of interconversion between CHD and HT after their formation by an ultrafast photochemical reaction. The photoexcited molecules that return to the ground state have sufficient internal energy to surmount the potential barriers, so that CHD–HT interconversion may occur in addition to the rotational isomerization of HT discussed earlier. Ruddock *et al.* investigated CHD–HT interconversion by exciting CHD to the 3p Rydberg state at 200 nm (6.2 eV), rather than to the S_1 state excited at 267 nm, and they followed the structural evolution using ultrafast X-ray diffraction up to a delay time as long as 1 ns.[43] Since the photoexcited Rydberg state of

CHD undergoes internal conversion to the ground state within several hundred femtoseconds, the X-ray scattering signals at delay times from picoseconds to 1 ns are primarily from highly vibrationally excited CHD and HT molecules in S_0. Fig. 11(a) shows the time-dependent X-ray scattering signal in two selected regions of the transferred momentum q (corresponding to s in electron diffraction). The rapid change within 1 ps is attributed to a ring-opening reaction to produce HT and non-reactive internal conversion to CHD from the Rydberg state, and both processes are complete well within 1 ps. Surprisingly, the diffraction

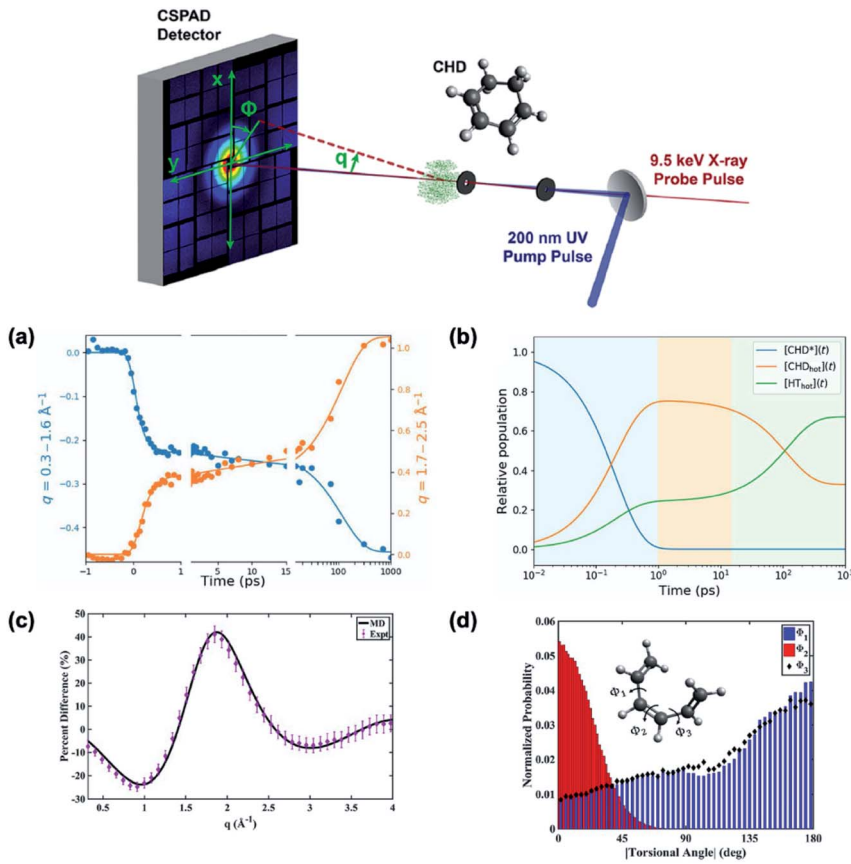

Fig. 11 Ultrafast X-ray diffraction. (a) Experimental percentage difference scattering signal after 200 nm photoexcitation of CHD measured as a function of the pump–probe time delay. Plotted are averages over two momentum transfer vector (q) ranges (dots) and the kinetic fits (lines). q is given by $2k_0 \sin\theta$ where k_0 is the incident wave vector and θ is the scattering angle. (b) Relative populations of the three components on a logarithmic timescale: electronically excited CHD*, the vibrationally excited ground state CHD_{hot}, and the vibrationally excited ground state HT_{hot}. The background colours indicate the different time regimes of the kinetics: blue is dominated by the decay of CHD*, orange is dominated by CHD_{hot}, and green indicates the equilibration to 67% HT_{hot} and 33% CHD_{hot}. (c) Percentage difference scattering pattern for hot HT. Experimental data points are indicated with purple dots, and the scattering pattern calculated using molecular dynamics simulation is indicated by a black solid line. (d) Histogram of the three torsional angles in HT used for simulating the scattering pattern shown in (c). Adapted from ref. 43 and 92.

intensities in the two different regions continuously change, which points to a slow isomerization reaction in S_0. Ruddock *et al.* analysed the time-dependent X-ray scattering distribution, $P(q,t)$, as an incoherent sum of the scattering signals from different chemical structures, as expressed by the following equation,

$$P(q,t) = [\mathrm{CHD}^*(t)]S_{\mathrm{CHD}^*}(q) + [\mathrm{CHD}_{\mathrm{hot}}(t)]S_{\mathrm{CHDhot}}(q) + [\mathrm{HT}_{\mathrm{hot}}(t)]S_{\mathrm{HThot}}(q)$$

where $[\mathrm{CHD}^*(t)]$, $[\mathrm{CHD}_{\mathrm{hot}}(t)]$, and $[\mathrm{HT}_{\mathrm{hot}}(t)]$ are the time-dependent populations of CHD in the Rydberg state, vibrationally excited CHD produced by internal conversion to the ground state, and the HT product in the ground state, respectively. $S_{\mathrm{CHD}^*}(q)$, $S_{\mathrm{CHDhot}}(q)$, and $S_{\mathrm{HThot}}(q)$ are the associated time-independent scattering patterns. By least squares fitting of time-dependent diffraction signals, they extracted the individual population and scattering patterns for the three species. The time-dependent populations shown in Fig. 11(b) indicate that the reaction starting from the Rydberg state predominantly populates the ground state of CHD rather than HT, while isomerization from the former to the latter ultimately reverses their populations. $S_{\mathrm{HThot}}(q)$ determined by the least squares fitting of the time-dependent diffraction pattern is shown as purple dots in Fig. 11(c). Ruddock *et al.* compared the extracted diffraction patterns with those computationally predicted using nuclear trajectory calculations on the ground-state potential energy surface and the IAM (black solid line),[92] and they found good agreement between them. The distribution of Φ_1, Φ_2 and Φ_3 in hot HT calculated using molecular dynamics simulations is shown in Fig. 11(d),[92] which reveals a quite broad probability density distribution, as anticipated for highly vibrationally excited molecules. This work is perhaps one of a few studies that followed slow isomerization processes on a sub-picosecond to nanosecond time scale under collision-free conditions. This study also demonstrated that X-ray diffraction can capture a minute change in the electron density distribution in CHD upon single electron excitation to a Rydberg orbital.

III. Photochemical reactions in crystals and solutions

It is of great interest to study *in situ* the photoinduced dynamics of molecules that play a key role in biological processes. However, one of the obvious problems is that if a photochemical reaction occurs irreversibly, the same sample cannot be employed for repeat measurements, and the sample needs to be replaced for each subsequent measurement. Serial femtosecond crystallography[93] overcomes this difficulty by introducing a stream of minute crystals for X-ray diffraction measurements. An intense X-ray pulse from an XFEL is diffracted before the sample breaks apart (diffraction-before-destruction principle), and a fresh crystalline sample is delivered for each measurement. Therefore, this method enables studies on irreversible reactions and avoids the influence of radiation damage.[94] It might be thought that a crystalline environment is too rigid for a photochemical reaction to occur; however, crystals of biological macromolecules contain sufficient internal space and are flexible enough for structural changes to occur upon photoexcitation.

Photoreactive yellow protein (PYP) is a blue-light photoreceptor for negative phototaxis of the purple phototrophic bacterium *Halorhodospira halophila*. The

function of PYP is expressed through *trans–cis* photoisomerization of its chromophore, *p*-coumaric acid (*p*CA), which triggers conformational change of the protein on a millisecond time scale. In an experiment with PYP, Pande *et al.* excited a microcrystal with 450 nm light pulses (140 fs) and measured the diffraction of 9 keV X-ray pulses (40 fs). They found that *p*CA undergoes *trans–cis* photoisomerization at around 590 fs.[95] The *p*CA molecule is covalently bonded to Cys69 in the side chain of PYP, and the phenolate oxygen ($O_{4'}$) of *p*CA is hydrogen-bonded to Glu46 and Tyr42. Prior to photoexcitation, the torsional angle (ϕ_{tail}) for the $C_2{=}C_3$ double bond is 172° (yellow filled circle in the plot shown in Fig. 12). 100–400 fs after photoexcitation, ϕ_{tail} becomes 136°, and the hydrogen bond length between *p*CA–$O_{4'}$ and Glu46 increases from 2.5 to 3.4 Å, which enables the molecule to undergo structural change more freely. In 400–1200 fs, ϕ_{tail} diminishes to 53°, and it ultimately becomes 35° at 3 ps (see Fig. 12). The hydrogen bond length between *p*CA–$O_{4'}$ and Glu46 also returns to 2.94 Å at 3 ps. Although the X-ray diffraction study did not differentiate the electronic states before and after the reaction, Pande *et al.* speculated that the system reaches the S_1/S_0 conical intersection at around 590 fs (the red and green background colours in Fig. 12 indicate the excited and ground states, respectively). This speculation is in accordance with the results of transient absorption spectroscopy, which indicated that the population decay of the excited state can be expressed using a multi-exponential function with a dominant lifetime component of 0.5–0.6 ps (50%).[96,97]

Compared with X-ray diffraction measurements of crystals, similar experiments for solutions are highly challenging, because solute molecules are distributed with unequal intermolecular distances and random orientations. Moreover, the large excess of solvent molecules also creates diffraction signals. The diffraction signal from a solution can be categorized into three components:

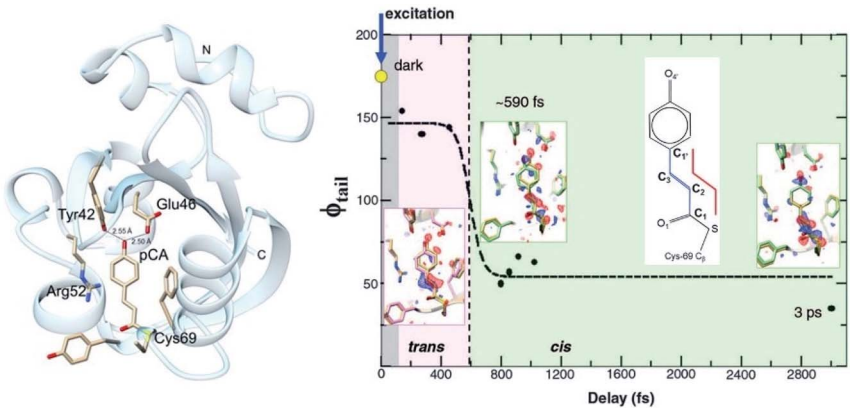

Fig. 12 Serial femtosecond crystallography: structure of *p*-coumaric acid (pCA) and measured torsional angle ϕ_{tail} for the C=C double bond. The pink region corresponds to the twisted *trans* form on the excited state potential energy surface (PES), and the light green region corresponds to the *cis* form on the ground state PES. Experimentally determined ϕ_{tail} values are indicated with solid spheres. The vertical dashed line indicates a transition time of about 590 fs. Insets: structures of PYP_{fast} (pink), PYP_{slow}, and PYP_{3ps} (light green), and the dark-state structure PYP_{ref} is indicated with a yellow sphere. The difference electron density is shown in the insets in red (-3σ) and blue (3σ). Adapted from ref. 95 and 98.

a solute-only component, a solute–solvent cross component, and a solvent-only component. The solute–solvent cross component depends on the interatomic distances between the solute and solvent molecules. The solvent-only component depends on the temperature and density of the solvent molecules, which are

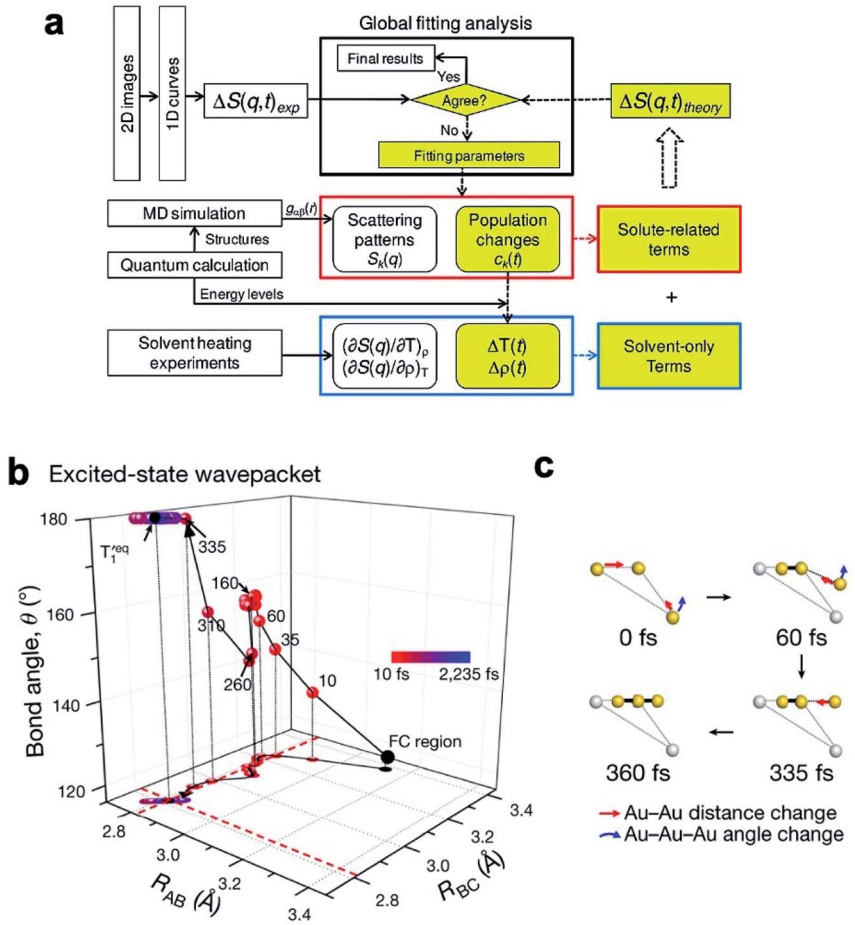

Fig. 13 Ultrafast X-ray liquidography (diffraction by a liquid sample): (a) standard procedure for data analysis. For details see ref. 99. The discrepancy between the experimental and simulation results is minimized using a global fitting method considering the data for all time delays simultaneously. Boxes in red and blue frames represent solute-related (solute-only and solute–solvent) and solvent-only components, respectively. Boxes with yellow background are involved in iterative adjustment. (b) Nuclear motion of Au atoms in the T'_1 excited state represented by the multidimensional nuclear coordinates R_{AB} *versus* R_{BC} *versus* θ. The projection onto the R_{AB}–R_{BC} plane is shown at the bottom. The equilibrium distances for R_{AB} and R_{BC} in T'_1 and S_0 are indicated by the red dashed lines. The colours of the dots represent the time delays shown on the colour scale. (c) Transient structures at representative time delays are illustrated, in which Au atoms at each time delay are represented by yellow dots, and those in the FC region are represented by grey dots. The black solid lines in (c) indicate covalent bonds. The changes in interatomic distance and angle are indicated by red and blue arrows, respectively. The ligands are omitted for simplicity. Structural changes are exaggerated for clarity. Adapted from ref. 99 and 100.

altered by energy transfer from photoexcited solute molecules or photoexcitation of the solvent itself. Analysis of the highly complex diffraction signal from a solution sample is only possible with extensive computational (quantum chemistry and molecular dynamics) simulations as depicted in Fig. 13(a).[99] Nonetheless, with regard to the photochemistry of the dicyanoaurate trimer, $[Au(CN)_2]_3^-$, the analysis was drastically simplified. What was highly favourable for this experiment was that the scattering signal from the Au atoms was so strong that the scattering from the C and N atoms and the solute–solvent cross component were negligible. Only the solvent-only component, which is due to heating by intermolecular energy transfer from the solute, was considered. The dicyanoaurate trimer is weakly bound in the electronic ground state by aurophilicity, which originates from relativistic effects in the electronic structure of Au atoms and provides a bonding strength comparable with that for hydrogen bonds. Electron promotion from the anti-bonding $\sigma^*(d_{z^2}–d_{z^2})$ to the bonding $\sigma(p_x–p_x)$ molecular orbitals triggers formation of covalent bonds in the excited state. Kim *et al.* photoexcited $[Au(CN)_2]_3^-$ in an aqueous solution to the S_1 state with 267 nm pulses and followed the subsequent structural transformation using X-ray diffraction with 12.7 (or 15) keV pulses. Although the dimer concentration was two times higher than that of the trimer, the extinction coefficient for the dimer was 27 times smaller than that for the trimer, so the contribution of the dimer was considered negligible. The FWHM of instrumental response function was 170–320 fs, depending on the facility (PAL or SACLA). Fig. 13(b) shows the bond lengths and bond angles between the three Au atoms in the trimer determined as a function of time.[100] It can be seen that the first Au–Au bond is formed within 60 fs, and the second bond is formed in about 300 fs. During formation of the covalent bonds, the configuration of the three Au atoms changes from a bent to a linear structure (Fig. 13(c)). These remarkable experimental results highlight the high potential of ultrafast X-ray diffraction experiments on solutions made possible using XFELs. One note is that this reaction has also been investigated using optical spectroscopic methods, such as transient absorption,[101] emission,[102] and stimulated Raman scattering,[103] and there are some controversies regarding the assignment of the electronic states and the reaction times. These points are expected to be clarified in the near future.

In transient absorption spectroscopy of solutions, a comprehensive analysis is often performed on electronic spectra in the visible/UV region and vibrational spectra in the infrared region. Similarly, X-ray absorption and infrared spectroscopies provide complementary information on the electronic and structural dynamics. Ferrioxalate $[Fe(III)(C_2O_4)_3]^{3-}$ is known to undergo a rapid photochemical reaction under sunlight and induces decomposition of contaminants in water. The reaction is also employed as a chemical actinometer. The reaction is often expressed as,

$$2[Fe(III)(C_2O_4)_3]^{3-} + h\nu \rightarrow 2[Fe(II)(C_2O_4)_2]^{2-} + 2CO_2 + C_2O_4^{2-}$$

However, the elementary reaction mechanism was controversial.[104–108] Ogi *et al.,* studied this reaction using transient absorption spectroscopy in the hard X-ray region using an XFEL. They excited a 0.1 M aqueous solution of ferrioxalate

with 268 nm pulses and observed the absorption spectrum at the K-edge of iron (7.1 keV) with a time resolution of 200 fs.[109] Fig. 14(a) compares the X-ray absorption spectra of the solution before (black, −3 ps) and after (blue, 7 ps) UV irradiation, and the spectrum of the photoproducts (red) extracted using spectral analysis. The absorption edge for the product was 6 eV lower than that for the reactant, indicating that the Fe atoms were reduced. The continuous absorption in the energy region above the absorption edge exhibits oscillatory features, which are due to quantum mechanical interference of outgoing photoelectron waves scattered by oxygen atoms adjacent to Fe. From these features, the iron–oxygen bond lengths in the product were estimated to be 2.04 Å. Fig. 14(b) shows time profiles measured at different X-ray photon energies, which indicate a decrease in the parent signal and immediate appearance of the red-shifted

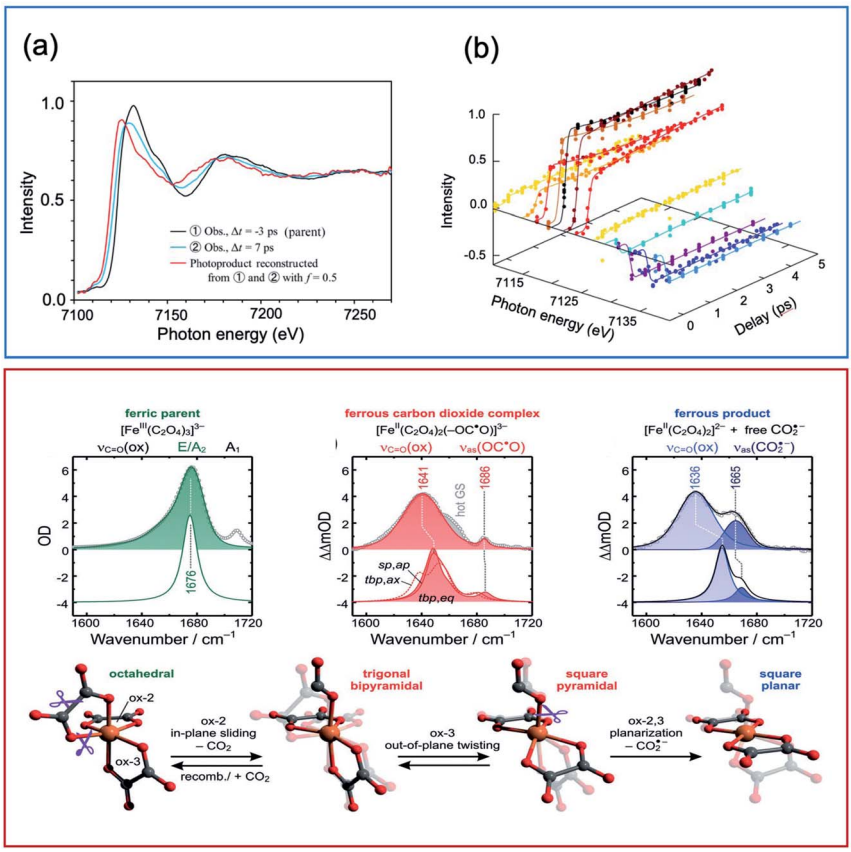

Fig. 14 Transient X-ray and infrared absorption spectroscopy: (a) reconstructed spectrum of the photoproduct (red) generated from the static spectrum of $[Fe^{III}(C_2O_4)_3]^{3-}$ ($S = 5/2$) (black) and the spectrum measured at $t = 7$ ps (blue). (b) Time profiles of the X-ray fluorescence intensities excited at different X-ray photon energies and a global fit of the exponential decay curves (solid lines) measured as a function of time delay after irradiation by 268 nm pulses. (c) Schematic reaction mechanism for ferrioxalate, and experimental (upper graphs, symbols) and theoretical infrared spectra (lower graphs) for the ferrioxalate parent, the isomers of the ferrous carbon dioxide primary complex, and the final ferrous dioxalate product together with a free CO_2^- radical anion. Adapted from ref. 109 and 112.

absorption spectrum of the photoproduct. From these results, they concluded that the product was formed within 140 fs after photoexcitation. Based on the spectral redshift and Fe–O distance predicted by time-dependent density functional theory calculations, it was concluded that ligand-to-metal charge transfer (LMCT) induces CO_2 release from one of the ligands to produce $[(CO_2^{\cdot})Fe(II)(C_2O_4)_2]^{3-}$. The LMCT reduces the charge of the oxalate ligand from -2 to -1, which destabilizes the ligand and induces dissociation of a neutral CO_2 molecule. The remaining CO_2^- ligand is only weakly coordinated to Fe, so the product is expected to dissociate into $[Fe(II)(C_2O_4)_2]^{2-}$ and a CO_2^- radical anion. However, the yield and reaction time of this secondary dissociation process could not be determined using X-ray absorption spectroscopy with a limited observation time window in limited beam time. Later, transient infrared absorption spectroscopy performed by Mangiante *et al.* and Straub *et al.* unambiguously confirmed production of neutral CO_2 within the response time (< several hundred femtoseconds) of the infrared spectrometer,[110–112] in agreement with the X-ray experiment. Moreover, ejection of CO_2^- radical anions in a nanosecond time scale was confirmed. Fig. 14(c) shows the signature of CO_2 radical anions (the blue-coloured peak at 1665 cm^{-1}) observed after 1 ns. Infrared spectroscopy showed that 35% of the photoexcited ferrioxalate undergoes non-reactive internal conversion to the ground state and 65% undergoes dissociation to produce neutral CO_2.[111,112]

IV. Summary

In this paper, I presented a brief overview of some recent experimental studies in this field as an introductory lecture for the *Faraday Discussion* on "time-resolved imaging of photo-induced dynamics". Chemical reaction dynamics involve both electronic and structural dynamics, and there is no experimental methodology that can reveal all aspects of these dynamics in a single experiment. Different experimental methodologies provide complementary information, so their comprehensive analysis is invaluable. It is also highly desirable to compare experimental results with theoretical and computational simulations, such as high-precision quantum chemical calculations and molecular dynamics simulations, for interpretation of the experimental results. The computational methods are now at a sufficient level of accuracy to provide (semi-)quantitative replication and prediction of experimental results. Computational demand will further increase in order to deal with more complex systems, in which machine learning or the use of assistive intelligence will be sought.

The experimental methods to track the reaction from start to finish are inherently "universal" in the detection of molecules, and they are inevitably sensitive to unexcited reactant molecules in the ground state. For example, XUV probe pulses ionize the reactants to produce photoelectrons, and electron/X-ray pulses are scattered by the reactants to produce diffraction signals, even in the absence of pump pulses. If only 1% of reactant molecules are photoexcited by pump pulses, 99% of the signal caused by probe pulses arises from unexcited reactant molecules. Experiments are even more challenging for solutions, as the solvent also produces a signal. Thus, the common technical challenge in these experiments is extraction of a small signal of interest. High stability and a high repetition rate for pulsed photon/electron beam sources provide good statistics for signals and assist in

performing successful measurements. The Linac Coherent Light Source (LCLS) is being upgraded to LCLS-II, and the repetition rate will increase by four orders of magnitude from the current 120 Hz to 1 MHz. The Extreme Light Infrastructure (ELI) is a similarly large laser project launched in Europe, and it will offer user facilities for high-field physics and ultrafast laser science.[113] ELI-ALPS (ELI attosecond light pulse source) has already started offering light sources producing XUV attosecond pulses.[113] The achievement of higher repetition rates is a common goal for technical development of all quantum beam sources including these large-scale facilities and table-top systems.

Besides such large-scale facilities, HHG has had a great impact on many laboratory experiments. Thanks to advances in laser technology and industrial manufacturing, compact turn-key Ti:sapphire laser systems are now commercially available, and they deliver pulses with durations of 30 fs and energy greater than 5 mJ at a 1 kHz repetition rate. These lasers enable straightforward implementation of HHG-based XUV light sources in the laboratory. However, attosecond light sources using carrier envelope phase control and soft X-ray generation using near IR drivers require expertise and/or much investment at this point. Optical parametric chirped pulse amplifiers are employed in a limited number of advanced laboratories. These technologies, however, will become more accessible for many researchers in the future. Ti:sapphire driving lasers are gradually changing to alternatives such as Yb-based lasers with low thermal effects, and the capability to achieve high repetition rates up to the megahertz range. Such new laser systems will certainly improve the performance of laser spectroscopy and expand opportunities for exploring new aspects of the photophysical and photochemical dynamics of molecules.

Advanced facilities certainly offer exciting research opportunities. However, it should also be stressed to young people that not all great scientific discoveries are made at large advanced facilities. Dr Donna Strickland received the Nobel Prize in Physics in 2018 for chirped pulse amplification, which she studied in the laboratory during graduate school. Young people certainly have chances for great discoveries in laboratory work every day. I remember a famous joke that one of my professors told me many years ago, when I was a graduate student. This story is sometimes called "the streetlight effect". The story goes like this. A policeman sees a man searching for something under a streetlight and asks what he has lost. The man says he lost his key (or it could be a coin). They both look for it under the streetlight but they cannot find it. Then, the policeman asks if the man is sure he lost it here, and the man replies, no, he lost it elsewhere. Then, the policeman asks why he is searching here, and the man replies, "this is where the light is." The intention of the professor who introduced me to this story was perhaps to convey the stance that researchers should not take. Young students and researchers have great opportunities in research driven by their curiosity and courage to search in dark places.

The invited and contributed papers of this *Faraday Discussion* present cutting-edge research in this exciting research field and will certainly be inspirational to the participants at the meeting and many other readers of these papers and the records of the discussion.

Conflicts of interest

There are no conflicts to declare.

Acknowledgements

I gratefully appreciate the efforts of the organizers to make this *Faraday Discussion* possible as an internet conference at such a difficult time for mankind during the COVID-19 pandemic. I also express my gratitude to Professor Andrew Orr-Ewing and Dr Daisuke Koyama for measuring (unpublished) transient infrared absorption spectra for the photochemical reaction of the ferrioxalate complex. Financial support by JSPS KAKENHI (Grant Number 15H05753) and the Mitsubishi Foundation is appreciated.

References

1 M. Adrian, J. Dubochet, J. Lepault and A. W. McDowall, *Nature*, 1984, **308**, 32–36.
2 Y. F. Cheng, *Science*, 2018, **361**, 876–880.
3 R. Henderson, J. M. Baldwin, T. A. Ceska, F. Zemlin, E. Beckmann and K. H. Downing, *J. Mol. Biol.*, 1990, **213**, 899–929.
4 T. Nakane, A. Kotecha, A. Sente, G. McMullan, S. Masiulis, P. Brown, I. T. Grigoras, L. Malinauskaite, T. Malinauskas, J. Miehling, T. Uchanski, L. B. Yu, D. Karia, E. V. Pechnikova, E. de Jong, J. Keizer, M. Bischoff, J. McCormack, P. Tiemeijer, S. W. Hardwick, D. Y. Chirgadze, G. Murshudov, A. R. Aricescu and S. H. W. Scheres, *Nature*, 2020, **587**, 152–156.
5 K. M. Yip, N. Fischer, E. Paknia, A. Chari and H. Stark, *Nature*, 2020, **587**, 157–161.
6 G. Binning, H. Rohrer, C. Gerber and E. Weibel, *Phys. Rev. Lett.*, 1982, **49**, 57–61.
7 G. Binnig, C. F. Quate and C. Gerber, *Phys. Rev. Lett.*, 1986, **56**, 930–933.
8 J. Lee, K. T. Crampton, N. Tallarida and V. A. Apkarian, *Nature*, 2019, **568**, 78–82.
9 S. Duan, G. J. Tian and Y. Luo, *Angew. Chem., Int. Ed.*, 2016, **55**, 1041–1045.
10 J. Duris, S. Q. Li, T. Driver, E. G. Champenois, J. P. MacArthur, A. A. Lutman, Z. Zhang, P. Rosenberger, J. W. Aldrich, R. Coffee, G. Coslovich, F. J. Decker, J. M. Glownia, G. Hartmann, W. Helml, A. Kamalov, J. Knurr, J. Krzywinski, M. F. Lin, M. Nantel, A. Natan, J. O'Neal, N. Shivaram, P. Walter, A. L. Wang, J. J. Welch, T. J. A. Wolf, J. Z. Xu, M. F. Kling, P. H. Bucksbaum, A. Zholents, Z. R. Huang, J. P. Cryan, A. Marinelli and J. P. Marangos, *Nat. Photonics*, 2020, **14**, 30–36.
11 F. Krausz and M. Ivanov, *Rev. Mod. Phys.*, 2009, **81**, 163–234.
12 *Attosecond and XUV Physics: Ultrafast Dynamics and Spectroscopy*, *ed.* T. Schultz and M. Vrakking, Wiley-VCH, Weinheim, Germany, 2014.
13 Y. Morimoto and P. Baum, *Nat. Phys.*, 2018, **14**, 252–256.
14 A. Ryabov, J. W. Thurner, D. Nabben, M. V. Tsarev and P. Baum, *Sci. Adv.*, 2020, **6**, eabb1393.
15 P. M. Felker and A. H. Zewail, *Phys. Rev. Lett.*, 1984, **53**, 501–504.
16 P. M. Kraus, B. Mignolet, D. Baykusheva, A. Rupenyan, L. Horny, E. F. Penka, G. Grassi, O. I. Tolstikhin, J. Schneider, F. Jensen, L. B. Madsen, A. D. Bandrauk, F. Remacle and H. J. Worner, *Science*, 2015, **350**, 790–795.
17 P. B. Corkum and F. Krausz, *Nat. Phys.*, 2007, **3**, 381–387.

18 P. M. Kraus, M. Zurch, S. K. Cushing, D. M. Neumark and S. R. Leone, *Nat. Rev. Chem.*, 2018, **2**, 82–94.
19 M. Nisoli, P. Decleva, F. Calegari, A. Palacios and F. Martin, *Chem. Rev.*, 2017, **117**, 10760–10825.
20 A. H. Zewail, *J. Phys. Chem. A*, 2000, **104**, 5660–5694.
21 A. H. Zewail, *Science*, 2010, **328**, 187–193.
22 M. Galli, V. Wanie, D. P. Lopes, E. P. Mansson, A. Trabattoni, L. Colaizzi, K. Saraswathula, A. Cartella, F. Frassetto, L. Poletto, F. Legare, S. Stagira, M. Nisoli, R. M. Vazquez, R. Osellame and F. Calegari, *Opt. Lett.*, 2019, **44**, 1308–1311.
23 P. B. Corkum, *Phys. Rev. Lett.*, 1993, **71**, 1994–1997.
24 J. L. Krause, K. J. Schafer and K. C. Kulander, *Phys. Rev. Lett.*, 1992, **68**, 3535–3538.
25 R. Schoenlein, T. Elsaesser, K. Holldack, Z. R. Huang, H. Kapteyn, M. Murnane and M. Woerner, *Philos. Trans. R. Soc. A*, 2019, **377**, 20180384.
26 R. W. Schoenlein, S. Chattopadhyay, H. H. W. Chong, T. E. Glover, P. A. Heimann, C. V. Shank, A. A. Zholents and M. S. Zolotorev, *Science*, 2000, **287**, 2237–2240.
27 S. Khan, K. Holldack, T. Kachel, R. Mitzner and T. Quast, *Phys. Rev. Lett.*, 2006, **97**, 074801.
28 P. Beaud, S. L. Johnson, A. Streun, R. Abela, D. Abramsohn, D. Grolimund, F. Krasniqi, T. Schmidt, V. Schlott and G. Ingold, *Phys. Rev. Lett.*, 2007, **99**, 174801.
29 E. J. Heller, *Acc. Chem. Res.*, 1981, **14**, 368–375.
30 M. Chergui and E. Collet, *Chem. Rev.*, 2017, **117**, 11025–11065.
31 *Conical Intersections: Electronic Structure, Dynamics & Spectroscopy*, *ed.* W. Domcke, D. R. Yarkony and H. Koppel, World Scientific, Singapore, 2004.
32 B. G. Levine and T. J. Martinez, *Annu. Rev. Phys. Chem.*, 2007, **58**, 613–634.
33 S. Matsika and P. Krause, *Annu. Rev. Phys. Chem.*, 2011, **62**, 621–643.
34 *Conical Intersections: Theory, Computation and Experiment*, *ed.* W. Domcke, D. R. Yarkony and H. Koppel, World Scientific, Singapore, 2011.
35 R. B. Woodward and R. Hoffmann, *Angew. Chem., Int. Ed. Engl.*, 1969, **8**, 781–932.
36 S. Deb and P. M. Weber, *Annu. Rev. Phys. Chem.*, 2011, **62**, 19–39.
37 B. C. Arruda and R. J. Sension, *Phys. Chem. Chem. Phys.*, 2014, **16**, 4439–4455.
38 W. T. Van der Lugt and L. J. Oosterhoff, *Chem. Commun.*, 1968, 1235–1236.
39 C. J. Pedersen, *Angew. Chem., Int. Ed.*, 1988, **27**, 1021–1027.
40 R. Noyori, *Adv. Synth. Catal.*, 2003, **345**, 15–32.
41 A. A. Ischenko, P. M. Weber and R. J. D. Miller, *Chem. Rev.*, 2017, **117**, 11066–11124.
42 B. Stankus, H. W. Yong, N. Zotev, J. M. Ruddock, D. Bellshaw, T. J. Lane, M. N. Liang, S. Boutet, S. Carbajo, J. S. Robinson, W. P. Du, N. Goff, Y. Chang, J. E. Koglin, M. P. Minitti, A. Kirrander and P. M. Weber, *Nat. Chem.*, 2019, **11**, 716–721.
43 J. M. Ruddock, H. W. Yong, B. Stankus, W. P. Du, N. Goff, Y. Chang, A. Odate, A. M. Carrascosa, D. Bellshaw, N. Zotev, M. N. Liang, S. Carbajo, J. Koglin, J. S. Robinson, S. Boutet, A. Kirrander, M. P. Minitti and P. M. Weber, *Sci. Adv.*, 2019, **5**, eaax6625.

44 J. Yang, X. L. Zhu, J. P. F. Nunes, J. K. Yu, R. M. Parrish, T. J. A. Wolf, M. Centurion, M. Guhr, R. K. Li, Y. S. Liu, B. Moore, M. Niebuhr, S. Park, X. Z. Shen, S. Weathersby, T. Weinacht, T. J. Martinez and X. J. Wang, *Science*, 2020, **368**, 885–889.
45 C. Rose-Petruck, R. Jimenez, T. Guo, A. Cavalleri, C. W. Siders, F. Raksi, J. A. Squier, B. C. Walker, K. R. Wilson and C. P. J. Barty, *Nature*, 1999, **398**, 310–312.
46 G. Sciaini and R. J. D. Miller, *Rep. Prog. Phys.*, 2011, **74**, 096101.
47 C. I. Blaga, J. L. Xu, A. D. DiChiara, E. Sistrunk, K. K. Zhang, P. Agostini, T. A. Miller, L. F. DiMauro and C. D. Lin, *Nature*, 2012, **483**, 194–197.
48 L. Y. Ma, H. W. Yong, J. D. Geiser, A. M. Carrascosa, N. Goff and P. M. Weber, *Struct. Dyn.*, 2020, **7**, 034102.
49 L. S. Bartell, L. O. Brockway and R. H. Schwendeman, *J. Chem. Phys.*, 1955, **23**, 1854–1859.
50 R. Schoenlein, T. Elsaesser, K. Holldack, Z. R. Huang, H. Kapteyn, M. Murnane and M. Woerner, *Philos. Trans. R. Soc. A*, 2019, **377**, 20180384.
51 T. Suzuki, *Annu. Rev. Phys. Chem.*, 2006, **57**, 555–592.
52 L. Wang, H. Kohguchi and T. Suzuki, *Faraday Discuss.*, 1999, **113**, 37–46.
53 A. Stolow, A. E. Bragg and D. M. Neumark, *Chem. Rev.*, 2004, **104**, 1719–1757.
54 I. V. Hertel and W. Radloff, *Rep. Prog. Phys.*, 2006, **69**, 1897–2003.
55 M. Seel and W. Domcke, *J. Chem. Phys.*, 1991, **95**, 7806–7822.
56 T. Fuji, T. Horio and T. Suzuki, *Opt. Lett.*, 2007, **32**, 2481–2483.
57 T. Horio, T. Fuji, Y. I. Suzuki and T. Suzuki, *J. Am. Chem. Soc.*, 2009, **131**, 10392–10393.
58 T. Horio, R. Spesyvtsev and T. Suzuki, *Opt. Lett.*, 2014, **39**, 6021–6024.
59 T. Horio, R. Spesyvtsev, K. Nagashima, R. A. Ingle, Y. Suzuki and T. Suzuki, *J. Chem. Phys.*, 2016, **145**, 044306.
60 E. T. Sevy, M. A. Muyskens, S. M. Rubin, G. W. Flynn and J. T. Muckerman, *J. Chem. Phys.*, 2000, **112**, 5829–5843.
61 M. Sala, B. Lasorne, F. Gatti and S. Guerin, *Phys. Chem. Chem. Phys.*, 2014, **16**, 15957–15967.
62 W. W. Xie, M. Sapunar, N. Doslic, M. Sala and W. Domcke, *J. Chem. Phys.*, 2019, **150**, 154119.
63 M. Kanno, Y. Ito, N. Shimakura, S. Koseki, H. Kono and Y. Fujimura, *Phys. Chem. Chem. Phys.*, 2015, **17**, 2012–2024.
64 B. Mignolet, M. Kanno, N. Shimakura, S. Koseki, F. Remacle, H. Kono and Y. Fujimura, *Chem. Phys.*, 2018, **515**, 704–709.
65 M. Hackmeyer and J. L. Whitten, *J. Chem. Phys.*, 1971, **54**, 3739–3750.
66 K. Sun, W. Xie, L. Chen, W. Domcke and M. Gelin, *J. Chem. Phys.*, 2020, **153**, 174111.
67 S. P. Neville, M. Chergui, A. Stolow and M. S. Schuurman, *Phys. Rev. Lett.*, 2018, **120**, 243001.
68 T. Northey, J. Norell, A. E. A. Fouda, N. A. Besley, M. Odelius and T. J. Penfold, *Phys. Chem. Chem. Phys.*, 2020, **22**, 2667–2676.
69 S. Tsuru, M. L. Vidal, M. Papai, A. I. Krylov, K. B. Moller and S. Coriani, *J. Chem. Phys.*, 2019, **151**, 124114.
70 A. D. Smith, E. M. Warne, D. Bellshaw, D. A. Horke, M. Tudorovskya, E. Springate, A. J. H. Jones, C. Cacho, R. T. Chapman, A. Kirrander and R. S. Minns, *Phys. Rev. Lett.*, 2018, **120**, 183003.

71 R. J. Squibb, M. Sapunar, A. Ponzi, R. Richter, A. Kivimaki, O. Plekan, P. Finetti, N. Sisourat, V. Zhaunerchyk, T. Marchenko, L. Journel, R. Guillemin, R. Cucini, M. Coreno, C. Grazioli, M. Di Fraia, C. Callegari, K. C. Prince, P. Decleva, M. Simon, J. H. D. Eland, N. Doslic, R. Feifel and M. N. Piancastelli, *Nat. Commun.*, 2018, **9**, 63.
72 R. Al-Obaidi, M. Wilke, M. Borgwardt, J. Metje, A. Moguilevski, N. Engel, D. Tolksdorf, A. Raheem, T. Kampen, S. Mahl, I. Y. Kiyan and E. F. Aziz, *New J. Phys.*, 2015, **17**, 093016.
73 L. P. Oloff, M. Oura, K. Rossnagel, A. Chainani, M. Matsunami, R. Eguchi, T. Kiss, Y. Nakatani, T. Yamaguchi, J. Miyawaki, M. Taguchi, K. Yamagami, T. Togashi, T. Katayama, K. Ogawa, M. Yabashi and T. Ishikawa, *New J. Phys.*, 2014, **16**, 123045.
74 L. P. Oloff, K. Hanff, A. Stange, G. Rohde, F. Diekmann, M. Bauer and K. Rossnagel, *J. Appl. Phys.*, 2016, **119**, 225106.
75 J. H. Buss, H. Wang, Y. Xu, J. Maklar, F. Joucken, L. Zeng, S. Stoll, C. Jozwiak, J. Pepper, Y.-D. Chuang, J. D. Denlinger, Z. Hussain, A. Lanzara and R. A. Kaindl, *Rev. Sci. Instrum.*, 2019, **90**, 023105.
76 Y. Liu, J. E. Beetar, M. M. Hosen, G. Dhakal, C. Sims, F. Kabir, M. B. Etienne, K. Dimitri, S. Regmi, Y. Liu, A. K. Pathak, D. Kaczorowski, M. Neupane and M. Chini, *Rev. Sci. Instrum.*, 2020, **91**, 013102.
77 M. Puppin, Y. Deng, C. W. Nicholson, J. Feldl, N. B. M. Schroter, H. Vita, P. S. Kirchmann, C. Monney, L. Rettig, M. Wolf and R. Ernstorfer, *Rev. Sci. Instrum.*, 2019, **90**, 023104.
78 Y. Pertot, C. Schmidt, M. Matthews, A. Chauvet, M. Huppert, V. Svoboda, A. von Conta, A. Tehlar, D. Baykusheva, J. P. Wolf and H. J. Worner, *Science*, 2017, **355**, 264–267.
79 A. R. Attar, A. Bhattacherjee, C. D. Pemmaraju, K. Schnorr, K. D. Closser, D. Prendergast and S. R. Leone, *Science*, 2017, **356**, 54–58.
80 S. Karashima, A. Humeniuk, R. Uenishi, T. Horio, M. Kanno, T. Ohta, J. Nishitani, R. Mitric and T. Suzuki, 2021, submitted for publication.
81 I. Polyak, L. Hutton, R. Crespo-Otero, M. Barbatt and P. J. Knowles, *J. Chem. Theory Comput.*, 2019, **15**, 3929–3940.
82 A. H. Zewail, *Annu. Rev. Phys. Chem.*, 2006, **57**, 65–103.
83 M. BenNun, J. S. Cao and K. R. Wilson, *J. Phys. Chem. A*, 1997, **101**, 8743–8761.
84 T. J. A. Wolf, D. M. Sanchez, J. Yang, R. M. Parrish, J. P. F. Nunes, M. Centurion, R. Coffee, J. P. Cryan, M. Guhr, K. Hegazy, A. Kirrander, R. K. Li, J. Ruddock, X. Shen, T. Vecchione, S. P. Weathersby, P. M. Weber, K. Wilkin, H. Yong, Q. Zheng, X. J. Wang, M. P. Minitti and T. J. Martinez, *Nat. Chem.*, 2019, **11**, 504–509.
85 X. Shen, J. P. F. Nunes, J. Yang, R. K. Jobe, R. K. Li, M. F. Lin, B. Moore, M. Niebuhr, S. P. Weathersby, T. J. A. Wolf, C. Yoneda, M. Guehr, M. Centurion and X. J. Wang, *Struct. Dyn.*, 2019, **6**, 054305.
86 R. Improta, F. Santoro and L. Blancafort, *Chem. Rev.*, 2016, **116**, 3540–3593.
87 C. E. Crespo-Hernandez, B. Cohen, P. M. Hare and B. Kohler, *Chem. Rev.*, 2004, **104**, 1977–2019.
88 C. T. Middleton, K. de La Harpe, C. Su, Y. K. Law, C. E. Crespo-Hernandez and B. Kohler, *Annu. Rev. Phys. Chem.*, 2009, **60**, 217–239.
89 E. M. Arpa, M. M. Brister, S. J. Hoehn, C. E. Crespo-Hernandez and I. Corral, *J. Phys. Chem. Lett.*, 2020, **11**, 5156–5161.

90 R. Srinivasan, J. S. Feenstra, S. T. Park, S. J. Xu and A. H. Zewail, *Science*, 2005, **307**, 558–563.
91 M. F. Lin, Y. A. Dyakov, C. M. Tseng, A. M. Mebel, S. H. Lin, Y. T. Lee and C. K. Ni, *J. Chem. Phys.*, 2005, **123**, 054309.
92 H. W. Yong, J. M. Ruddock, B. Stankus, L. Y. Ma, W. P. Du, N. Goff, Y. Chang, N. Zotev, D. Bellshaw, S. Boutet, S. Carbajo, J. E. Koglin, M. N. Liang, J. S. Robinson, A. Kirrander, M. P. Minitti and P. M. Weber, *J. Chem. Phys.*, 2019, **151**, 084301.
93 L. C. Johansson, B. Stauch, A. Ishchenko and V. Cherezov, *Trends Biochem. Sci.*, 2017, **42**, 749–762.
94 H. Ki, K. Y. Oang, J. Kim and H. Ihee, *Annu. Rev. Phys. Chem.*, 2017, **68**, 473–497.
95 K. Pande, C. D. M. Hutchison, G. Groenhof, A. Aquila, J. S. Robinson, J. Tenboer, S. Basu, S. Boutet, D. P. DePonte, M. N. Liang, T. A. White, N. A. Zatsepin, O. Yefanov, D. Morozov, D. Oberthuer, C. Gati, G. Subramanian, D. James, Y. Zhao, J. Koralek, J. Brayshaw, C. Kupitz, C. Conrad, S. Roy-Chowdhury, J. D. Coe, M. Metz, P. L. Xavier, T. D. Grant, J. E. Koglin, G. Ketawala, R. Fromme, V. Srajer, R. Henning, J. C. H. Spence, A. Ourmazd, P. Schwander, U. Weierstall, M. Frank, P. Fromme, A. Barty, H. N. Chapman, K. Moffat, J. J. van Thor and M. Schmidt, *Science*, 2016, **352**, 725–729.
96 H. Kuramochi, S. Takeuchi, K. Yonezawa, H. Kamikubo, M. Kataoka and T. Tahara, *Nat. Chem.*, 2017, **9**, 660–666.
97 D. S. Larsen, I. H. M. van Stokkum, M. Vengris, M. A. van der Horst, F. L. de Weerd, K. J. Hellingwerf and R. van Grondelle, *Biophys. J.*, 2004, **87**, 1858–1872.
98 M. Schmidt, *Struct. Dyn.*, 2017, **4**, 032201.
99 H. Ihee, *Acc. Chem. Res.*, 2009, **42**, 356–366.
100 J. G. Kim, s. Nozawa, J. Kim, E. H. Choi, T. Sato, T. W. Kim, K. H. Kim, H. Ki, J. Kim, M. Choi, Y. Lee, J. Heo, K. Y. Oang, K. Ichiyanagi, R. Fukaya, J. H. Lee, J. Park, I. Eom, S. H. Chun, S. Kim, M. Kim, T. Katayama, T. Togashi, S. Owada, M. Yabashi, S. J. Lee, S. Lee, C. W. Ahn, D.-S. Ahn, J. Moon, S. Choi, J. Kim, T. Joo, J. Kim, S. Adachi and H. Ihee, *Nature*, 2020, **582**, 520–524.
101 M. Iwamura, R. Wakabayashi, J. Maeba, K. Nozaki, S. Takeuchi and T. Tahara, *Phys. Chem. Chem. Phys.*, 2016, **18**, 5103–5107.
102 S. H. Sohn, W. Heo, C. Lee, J. Kim and T. Joo, *J. Phys. Chem. A*, 2019, **123**, 6904–6910.
103 H. Kuramochi, S. Takeuchi, M. Iwamura, K. Nozaki and T. Tahara, *J. Am. Chem. Soc.*, 2019, **141**, 19296–19303.
104 J. Chen, H. Zhang, I. V. Tomov and P. M. Rentzepis, *Inorg. Chem.*, 2008, **47**, 2024–2032.
105 I. P. Pozdnyakov, O. V. Kel, V. F. Plyusnin, V. P. Grivin and N. M. Bazhin, *J. Phys. Chem. A*, 2008, **112**, 8316–8322.
106 J. Chen, A. S. Dvornikov and P. M. Rentzepis, *J. Phys. Chem. A*, 2009, **113**, 8818–8819.
107 I. P. Pozdnyakov, O. V. Kel, V. F. Plyusnin, V. P. Grivin and N. M. Bazhin, *J. Phys. Chem. A*, 2009, **113**, 8820–8822.

108 J. Chen, H. Zhang, I. V. Tomov, M. Wolfsherg, X. L. Ding and P. M. Rentzepis, *J. Phys. Chem. A*, 2007, **111**, 9326–9335.
109 Y. Ogi, Y. Obara, T. Katayama, Y. I. Suzuki, S. Y. Liu, N. C. M. Bartlett, N. Kurahashi, S. Karashima, T. Togashi, Y. Inubushi, K. Ogawa, S. Owada, M. Rubesova, M. Yabashi, K. Misawa, P. Slavicek and T. Suzuki, *Struct. Dyn.*, 2015, **2**, 034901.
110 D. M. Mangiante, R. D. Schaller, P. Zarzycki, J. F. Banfield and B. Gilbert, *ACS Earth Space Chem.*, 2017, **1**, 270–276.
111 S. Straub, P. Brunker, J. Lindner and P. Vohringer, *Phys. Chem. Chem. Phys.*, 2018, **20**, 21390–21403.
112 S. Straub, P. Brunker, J. Lindner and P. Vohringer, *Angew. Chem., Int. Ed.*, 2018, **57**, 5000–5005.
113 S. Kuhn, M. Dumergue, S. Kahaly, S. Mondal, M. Fule, T. Csizmadia, B. Farkas, B. Major, Z. Varallyay, F. Calegari, M. Devetta, F. Frassetto, E. Mansson, L. Poletto, S. Stagira, C. Vozzi, M. Nisoli, P. Rudawski, S. Maclot, F. Campi, H. Wikmark, C. L. Arnold, C. M. Heyl, P. Johnsson, A. L'Huillier, R. Lopez-Martens, S. Haessler, M. Bocoum, F. Boehle, A. Vernier, G. Iaquaniello, E. Skantzakis, N. Papadakis, C. Kalpouzos, P. Tzallas, F. Lepine, D. Charalambidis, K. Varju, K. Osvay and G. Sansone, *J. Phys. B: At., Mol. Opt. Phys.*, 2017, **50**, 132002.

